# Watching the release of a photopharmacological drug from tubulin using time-resolved serial crystallography

Maximilian Wranik[1], Tobias Weinert[1], Chavdar Slavov[2], Tiziana Masini[3], Antonia Furrer[1], Natacha Gaillard[1], Dario Gioia[3], Marco Ferrarotti[3], Daniel James[1], Hannah Glover[1], Melissa Carrillo[1], Demet Kekilli[1], Robin Stipp[1], Petr Skopintsev[1], Steffen Brünle[1], Tobias Mühlethaler[1], John Beale[1], Dardan Gashi[4], Karol Nass[4], Dmitry Ozerov[5], Philip J.M. Johnson[4], Claudio Cirelli[4], Camila Bacellar[4], Markus Braun[2], Meitian Wang[4], Florian Dworkowski[4], Chris Milne[4], Andrea Cavalli[3,6], Josef Wachtveitl[2], Michel O. Steinmetz[1,7,*], Jörg Standfuss[1,*]

[1] Division of Biology and Chemistry, Paul Scherrer Institut, 5232 Villigen, Switzerland.
[2] Institute of Physical and Theoretical Chemistry, Goethe University, Frankfurt am Main, Germany.
[3] Computational & Chemical Biology, Istituto Italiano di Tecnologia, 16163 Genova, Italy.
[4] Photon Science Division, Paul Scherrer Institut, 5232 Villigen, Switzerland.
[5] Scientific Computing, Theory and Data, Paul Scherrer Institut, 5232 Villigen, Switzerland.
[6] Department of Pharmacy and Biotechnology, University of Bologna, 40126 Bologna, Italy.
[7] Biozentrum, University of Basel, 4056 Basel, Switzerland.

*Correspondence to: michel.steinmetz@psi.ch and joerg.standfuss@psi.ch

**Abstract**

The binding and release of ligands from their protein targets is central to fundamental biological processes as well as to drug discovery. Photopharmacology introduces chemical triggers that allow the changing of ligand affinities and thus biological activity by light. Insight into the molecular mechanisms of photopharmacology is largely missing because the relevant transitions during the light-triggered reaction cannot be resolved by conventional structural biology. Using time-resolved serial crystallography at a synchrotron and X-ray free-electron laser, we captured the release of the anti-cancer compound azo-combretastatin A4 and the resulting conformational changes in tubulin. Nine structural snapshots from 1 ns to 100 ms complemented by simulations show how *cis*-to-*trans* isomerization of the azobenzene bond leads to a switch in ligand affinity, opening of an exit channel, and collapse of the binding pocket upon ligand release. The resulting global backbone rearrangements are related to the action mechanism of microtubule-destabilizing drugs.

## Introduction

The dynamic interaction of small molecule ligands with their target proteins is the basis for numerous physiological processes in living cells. To catalyze chemical reactions, enzymes have to bind their substrates and release the products. Cellular signaling is coordinated by the binding of ligands that activate their cognate receptors in the cytoplasm or the cellular membrane. Small molecule ligands that act as drugs to selectively intercede in these physiological processes provide the most common strategy for medical intervention.

Photopharmacology introduces photochemical triggers into small molecule ligands to be able to change binding affinities and manipulate complex biological processes with the help of light[1]. The most widely used photochemical affinity switches are based on the azobenzene scaffold that allows for high quantum efficiencies, fast trigger rates, and reversible photoisomerization upon illumination[2]. A prominent example is an azobenzene derivative of combretastatin A4 (azo-CA4)[3], a photopharmacological compound that binds the colchicine-site of the αβ-tubulin heterodimer (hereafter called tubulin)[4]. Tubulin is the key building block of the microtubule cytoskeleton in all eukaryotic cells and amongst others essential for cell division[5]. It is thus a common target for medically relevant agents including the first line anti-cancer drug paclitaxel (Taxol). While colchicine modulates multiple pro- and anti-inflammatory pathways associated with gouty arthritis[6], combretastatin A4 (CA4) is a strong cell growth inhibitor[7] that has been tested in clinical trials against different types of tumors[8, 9]. Interestingly, the phase III drug sabizabulin, that decreases mortality in intense-care COVID-19 patients by 55%[10], is also a colchicine-site ligand, sharing one binding moiety with combretastatins. The diverse applications of these small molecule drugs highlight the importance of the colchicine-site as a hotspot to influence the various cellular processes related to microtubule structure and function. A better understanding of how the dynamic interplay between a ligand and the colchicine-site is related to the conformational plasticity of tubulin may help further developments of this class of anti-tubulin agents for medical applications.

Besides its applications in photopharmacology[1] and material sciences[11], the azobenzene scaffold is also ideally suited for time-resolved pump-probe spectroscopy to understand protein motion[12]. Among the latest incarnations of the pump-probe technique is time-resolved serial crystallography to resolve molecular snapshots of proteins that can be assembled into stop-motion movies of how proteins function[13, 14]. The method has been most successful when studying photoactive proteins that are easy to trigger with high temporal precision; however, these represent less than 0.5% of all known proteins[15]. In order to reach the full potential of

time-resolved crystallography, new ways have to be developed to trigger protein-ligand interaction and protein dynamics in non-photoactive protein targets.

To this end, we show here how to utilize photopharmacological compounds to assess protein-ligand interaction dynamics and the resulting protein response over time. We first obtained the structure of azo-CA4 in complex with tubulin, before following its photoflash-induced release at the Swiss Light Source (SLS) and the Swiss X-ray Free Electron Laser (SwissFEL). We resolved the structural evolution at up to 1.7 Å spatial resolution in nine logarithmically-timed structural snapshots ranging from 1 ns to 100 ms. Our molecular snapshots show the formation and dissolution of a metastable, intermediate ligand-binding pose, and the accompanying reorganizations of the most frequently targeted drug-binding site in tubulin[16]. We anticipate that similar photoswitchable compounds developed to control kinases, channels, G protein-coupled receptors, and other pharmaceutically relevant protein targets will be important future tools to study protein-ligand interaction dynamics in non-photoactive protein targets at high spatial resolution and without compromising time resolution.

## Results

### Adapting photopharmacology for time-resolved serial crystallography

Time-resolved crystallography is ever more sample efficient (Supplementary Figure 1) and the technology is now available at a growing number of synchrotrons and X-ray free-electron lasers (XFELs)[17,18]. With increased availability of beamtime at these advanced X-ray sources, future challenges will shift towards enabling dynamic studies on a wide range of relevant biological targets. Photopharmacology could be an important part of the solution as the field already developed a variety of photosensitive compounds that can be utilized as efficient triggers to activate diverse soluble and membrane proteins of medical interest (for some examples, see Supplementary Figure 2).

In the last few years, tubulin-targeting photoswitches based on different scaffolds have been synthesized, for some of which we also obtained structures[19, 20]. To demonstrate the use of a photochemical affinity switch for time-resolved crystallography, we chose azo-CA4 as a prominent photopharmacological compound[21] with minimal modifications to the parent compound CA4. Replacing the central C=C stilbene bond found in CA4 with an N=N azobenzene bond in azo-CA4 results in a shift of the absorption maximum out of the ultraviolet range and in an increased photoreactivity. After the modification, illumination with blue or green light allows for reversible switching of the molecule between the high-affinity *cis* and low-affinity *trans* conformations, respectively[3]. This effect allows perturbing the division of cancer cells using a localized pulse of monochromatic light[3]. However, how azobenzene

110 isomerization changes binding affinity, how this induces structural adaptations within the
111 binding pocket, and how this then affects the global conformational plasticity of tubulin that is
112 needed during microtubule formation is largely unknown.
113 The idea behind our experiment was to use time-resolved crystallography to follow how the
114 ligand relaxes after photoactivation, allowing it to be observed bound to the protein in its out-
115 of-equilibrium, low affinity state, and eventually observe ligand unbinding and the resulting
116 changes in the protein (Figure 1). As a first step, we synthesized azo-CA4 and characterized its
117 tubulin-binding properties under crystallization conditions using the TD1 crystal system
118 composed of one αβ-tubulin heterodimer and one DARPin D1 molecule[22, 23] (Supplementary
119 Figure 3). Based on these results, we designed time-resolved crystallography experiments to
120 reveal the structural changes upon ligand isomerization and release.
121 Overall, we collected 1'139'945 indexable diffraction patterns with a resolution of up to 2.1 Å
122 when using serial synchrotron crystallography at the SLS[24, 25] and 1.7 Å when using serial
123 femtosecond crystallography at the SwissFEL[26] (Supplementary Table 1). The XFEL data are
124 divided into "dark" images collected without light exposure, images from crystals without
125 ligand, and pump-probe data taken at logarithmically spaced time delays of 1 ns, 10 ns, 100 ns,
126 1 μs, 10 μs, 100 μs, 1 ms, and 10 ms after illumination with flashes of laser light.
127 This untargeted approach relies on both synchrotron and XFEL setups to cover nine orders of
128 magnitude in time, which increases accessibility and remains an option even for cases where
129 initial spectroscopic data is scarce. We have characterized the ultrafast regime and initial
130 photochemical reaction using transient absorption spectroscopy (Supplementary Figure 3);
131 however, here we focus on the temporal domain starting from the nanoseconds where the
132 biochemically most relevant conformational changes in the protein are to be expected[18].
133 Difference electron density maps ($F_{obs}$(light)-$F_{obs}$(dark)) calculated from the time-resolved data
134 are of high quality (Figure 1D, Supplementary Figure 4, Supplementary Movie 1) and can be
135 qualitatively followed by Pearson correlation analysis to highlight transitions between
136 structural intermediates[27] (Figure 1B). We observed three major blocks of elevated correlation
137 compatible with a nonequilibrium photoproduct population that relaxes via several
138 intermediates into the ligand-free state of tubulin. Following the build-up of negative density
139 around azo-CA4 (Figure 1C) suggests that ligand release starts after the 1 ms delay at the end
140 of the second block observed in the Pearson correlation analysis. Using structural refinements
141 against extrapolated data from the light-activated fraction of the structure factors[28, 29], we were
142 able to generate atomic models for predominant intermediate states (Figure 1D, Supplementary

143 Table 2). In addition, we used conventional refinement approaches to obtain room temperature
144 crystal structures of tubulin in its *cis*-azo-CA4 bound and ligand-free states.
145 Together, these data provide a comprehensive overview of the structural changes occurring
146 after *cis-trans* isomerization and the following release of the azo-CA4 compound from its
147 tubulin binding pocket. A molecular movie obtained from morphing between these states
148 (Supplementary Movie 2) summarizes the critical molecular rearrangements that are described
149 in the following.
150
151 **Formation of a metastable binding pose after azo-CA4 photoisomerization**
152 The conformation of a ligand is generally presumed to precisely fit the architecture of its
153 binding pocket. The photoinduced release of azo-CA4 provides a system to study what happens
154 when a ligand deviates from its primary binding pose (Figure 2A). Before light-activation, the
155 *cis* isomer of azo-CA4 is bound to the colchicine site at the interface between the α and β
156 subunits of tubulin (Figure 1A). Interactions with the protein are primarily hydrophobic in
157 nature, except for hydrogen bonds to the backbone carbonyl of αThr179 and the backbone
158 amide of αVal181, respectively (Figure 2B). Further interactions are mediated by a water
159 molecule interacting directly with the azobenzene bond of azo-CA4. Overall, the binding pose
160 of the ligand is nearly identical to that of the parent compound CA4 that contains a stilbene
161 instead of the azobenzene group connecting the A and B rings of the ligand[4].
162 Transient absorption spectroscopy shows how illumination of azo-CA4 induces *cis-trans*
163 isomerization around the azobenzene bond, which is completed in the late picosecond range
164 following by its relaxation into the nanoseconds (Supplementary Figure 3). Our structures show
165 how the compound transitions from the partially disordered conformation observed in the 1 ns
166 time delay into a relaxed *trans*-azo-CA4 state observed at 100 ns after light activation. At this
167 point in time, the molecule is stretched by 2.2 Å, which relocates its A ring by 2.6 Å towards
168 the βT7 loop known to be involved in ligand unbinding[4, 23] (Figure 2C). Stretching along the
169 azobenzene bond changes the interaction pattern with the protein and the binding pocket. The
170 water-mediated interactions are broken and relocation of the two ring moieties of azo-CA4
171 reduces their hydrophobic stacking interactions with the protein.
172 To bridge the gap between structural effects and binding energy we relied on molecular
173 dynamics (MD) simulations[30]. We aimed at estimating the relative binding free energy
174 difference between the *cis* and *trans* isomers ($\Delta\Delta G_{cis\text{-}trans}$) using the computational protocol
175 utilized for the tubulin-combretastatin A4 complex[4]. As expected, the *trans* isomer is the most
176 stable form in both the bound and unbound simulations with ΔG values of $\Delta G_{cis\text{-}trans\text{-}bound}$ = -14

177 kcal/mol and $\Delta G_{cis\text{-}trans\text{-}unbound}$ = -19 kcal/mol, respectively. The resulting relative binding free
178 energy difference of $\Delta\Delta G_{cis\text{-}trans}$ = 5 kcal/mol clearly favors the *cis*-isomer stabilized interactions
179 with tubulin (free energy profiles are given in Supplementary Figure 5). Such a free energy
180 difference translates into an increased affinity of ~4300 times based on the equilibrium
181 probability ratio and Boltzmann statistics. This change is in good agreement with radioligand
182 scintillation proximity assays that indicated an $EC_{50}$ value of ~30 μM for illuminated azo-CA4
183 (representing a mixture of cis-trans isomers) but no significant competitive binding of the
184 relaxed *trans*-azo-CA4 to tubulin[3]. The low affinity of *trans*-CA4 also explains why we were
185 unable to crystallize this isomer in complex with tubulin using classical crystallography
186 methods but instead needed a time-resolved experiment to resolve the metastable binding pose
187 before azo-CA4 release.
188
189 **Binding pocket changes upon azo-CA4 release**
190 The colchicine site undergoes pronounced conformational changes between the ligand-bound
191 and -unbound states that are incompatible with a simple "lock-and-key" model of protein-ligand
192 interactions[4, 31, 32, 33]. In our time-resolved data, the relevant temporal regime starts at 100 ns,
193 when the A ring of the ligand has been repositioned into close contacts with residue βAla248
194 of the βT7 loop (Figure 3A). Initial conformational changes of the βT7 loop follow on the
195 microsecond scale with further rearrangements of the loop, including a displacement of
196 βAsn247 and βLeu246 occurring in the millisecond time range. The binding pocket initially
197 expands starting from a volume of 446 $Å^3$ before illumination (*cis*-azo-CA4) to 525 $Å^3$ at 100
198 ns (relaxed *trans*-azoCA4), and then collapses from 363 $Å^3$ at 1 ms (after βT7 loop movement)
199 down to 71 $Å^3$ at 10 ms when the compound has left the binding pocket. Based on visual
200 inspection of difference maps and plotting electron density changes on the ligand over time, we
201 have modeled the release of azo-CA4 between the 1 and 10 ms time delays (Figure 1C).
202 However, residual ligand can still be observed at low occupancy in the 10 ms data and is only
203 fully released at about 100 ms, where the structure is essentially identical to the one determined
204 in the absence of azo-CA4 (Supplementary Figure 6). The long release time is consistent with
205 a stochastic nature of the process where unbinding events of individual molecules occur over
206 several milliseconds in time once they are initiated on faster time scales.
207 The binding pocket is not freely accessible to the solvent but our structural analysis suggests
208 the opening of an exit channel between 100 μs and 1 ms (Figure 3B). Reorganization of the
209 βT7 loop, particularly through a rotation of the βLeu246 side chain, results into an 8 Å long
210 channel forming a possible exit site close to the A ring of the ligand (Figure 3C). The diameter

211 of the channel is 4-6 Å, which seems small given the 7 Å diameter for the larger A ring of azo-
212 CA4. As the unbinding takes place over many milliseconds throughout the crystal, it seems
213 likely that the channel transiently widens in short-lived intermediates that did not sufficiently
214 accumulate to be observed. To study this possibility, we have used MD simulations (Figure 3D)
215 starting from the 1 ms delay where the opening of the channel is most prominent. Almost 50 μs
216 of simulations (Supplementary Datasets 1 and 2) suggests that the azo-CA4 approaches a
217 position close to the proposed exit site of the protein, where only minimal changes would be
218 sufficient to let the ligand diffuse out of its binding pocket. Once the ligand detaches our
219 crystallographic data again shows how the βT7 loop flips back and packs against β-tubulin
220 residues that were previously engaged in azo-CA4 binding.
221 Together, these data are consistent with the flexible βT7 loop to act as a "molecular gate" that
222 opens and closes the colchicine site and, depending on its current conformation, directly
223 competes with ligand binding[32, 33]. Notably, all colchicine-site ligands must displace the βT7
224 loop upon binding[16, 34] as the pocket is contracted fully in ligand-free tubulin structures. Along
225 with the dynamic nature of the pocket at room temperature[24], this observation suggests
226 conformational selection as the predominant mechanism of how microtubule-destabilizing
227 agents interact with the colchicine-site.
228
229 **Global backbone rearrangements**
230 Tubulin displays substantial structural plasticity that is key to microtubule dynamics and thus
231 its cellular function. This includes the global conformation from a "curved" free tubulin to a
232 "straight" microtubule-lattice incorporated tubulin conformation[35]. This reorganization of the
233 tubulin dimer is accompanied by a contraction of the colchicine site[32, 33]. Ligand binding
234 prevents pocket contraction and thus stabilizes the curved conformation[16] as the principal action
235 mechanism for many tubulin-targeting anti-cancer drugs[16, 32, 33, 35].
236 To illustrate how global backbone rearrangements develop during the release of azo-CA4, we
237 superimposed our time-resolved structures and visualized the rearrangements of Cα backbone
238 atoms as individual vectors. We observed several motions that correspond well with our initial
239 Pearson-correlation analysis of electron density changes, and which coincide in time with the
240 major events in the ligand-binding pocket (Figure 4). Global structural changes are already
241 present in the nanosecond time range, where we observed coordinated inward motions of both
242 the α- and β-tubulin subunits (Figure 4A). These changes correlated well to the time range
243 where the A ring of azo-CA4 shifts to a new place completing the *cis*-to-*trans* relaxation process
244 within the binding pocket. Interestingly, some of these movements are reverted in the

245 microsecond time range, where the βT7 loop starts moving (Figure 4B). At this stage of the
246 reaction, global movements in the α and β subunits are directed predominately away from the
247 colchicine-site and may cause opening of ligand release pathway at 1 ms. In the later
248 millisecond range, where the βT7 loop finally collapses into the binding pocket, backbone
249 movements are primarily located in the α-tubulin subunit and bring the structure back to its
250 ligand-free state (Figure 4C).
251 To analyze whether the global backbone rearrangements could have an impact on the overall
252 conformation of microtubules, we analysed the curvature of an oligomer constructed from three
253 longitudinally, head-to-tail aligned tubulin dimers, as previously described[36]. Indeed, the
254 curvature is reduced significantly towards the direction of the straight protofilament
255 conformation found in microtubules once azo-CA4 is released. Our time-resolved structures
256 thus suggest that the global tubulin backbone movements, as well as overall changes in tubulin
257 conformational curvature evolve in par with structural alterations of the ligand that is bound to
258 the colchicine site.
259
260 **Discussion**
261 In the field of photopharmacology ligand design is done largely "blind" in the sense that little
262 is known about the molecular mechanism of how these modifications will alter dynamics and
263 activity of the target protein. In this context, it was reassuring to see that the interaction pattern
264 of the parent compound CA4 and the photoactive azo-CA4 remain largely the same. Further
265 knowledge of both the initial binding mode and the metastable binding pose after illumination
266 provides the molecular basis to understand differences in binding affinity between the *cis* and
267 *trans* forms of the compound. Together with molecular information on how the pocket adapts
268 during ligand release, this may provide innovative angles to improve the potency of azo-CA4
269 and perhaps other photopharmaceutical compounds.
270 In the wider context of general protein-ligand interaction dynamics, our work provides
271 molecular information beyond the classical "key and lock" model. The pharmaceutical industry
272 relies on such information as an integral part of a rational approach to discover new drugs and
273 understand their mechanisms of action. The colchicine-site is the most frequently targeted drug-
274 binding site in tubulin[16] with broad relevance to combat gout[6], cancer[7, 8, 9], and COVID-19[10].
275 Following the relaxation and release of the same ligand within different isoforms of tubulin[23]
276 or characterizing ligands specific for tubulin variants of parasitic origin[37] may offer new
277 avenues to rationally design innovative anti-tubulin ligands.

278 Finally, our study demonstrates how compounds developed for photopharmacology can be used
279 for time-resolved crystallography. While promising results using photo-caged compounds[38] and
280 rapid mixing have been shown[39, 40], these approaches will not allow observations on the fast
281 time scales relevant for protein-ligand interactions. It is furthermore difficult to predict how
282 ligands diffuse within a crystal, as this depends on crystal shape, size, packing and solvent
283 content among other parameters [41]. Starting a time-resolved experiment with a prebound ligand
284 is an elegant solution to the problem, even though it would be interesting to study to what extent
285 ligand binding and unbinding follow the same principles.
286 The underlying X-ray technology is now widely available, with many new endstations at 4$^{th}$
287 generation synchrotrons and XFELs purpose build for time-resolved pump-probe
288 measurements[17, 18]. The rapidly expanding field of photopharmacology delivers growing
289 numbers of photoswitches to, for example, modulate the activities of TRP channels, kinases, G
290 protein-coupled receptors, or to tackle antibiotic resistance[1, 11, 12, 42, 43, 44]. Together these
291 developments promise more direct experimental insights into the dynamic nature of protein-
292 ligand interactions in a wide range of relevant protein targets.
293
294 **Methods**
295 **Purification of tubulin-DARPin D1 complex**
296 Bovine brain tubulin was purchased from the Centro de Investigaciones Biológicas
297 (Microtubule Stabilizing Agents Group), CSIC, Madrid, Spain. DARPin D1 was expressed and
298 purified according to previous descriptions[22]. Detailed protocols for obtaining high-resolution
299 tubulin crystals can be found here[45].
300 Briefly, the pET-derived vector PSTCm9 includes the gene for the artificial DARPin D1 as a
301 N-terminal fusion with thioredoxin followed by a hexahistidine-tag and a thrombin cleavage
302 site. For expression the DARPin D1 carrying plasmid was transfected into competent E.coli
303 BL21 (DE3) cells and the protein expressed in LB medium in 2 L Erlenmeyer flask. The cells
304 were harvested by centrifugation at 5000 g and stored at 80 degrees Celsius.
305 The cell walls were lysed on ice using an ultrasonic cell disrupter applying alterations of 2 s on
306 and off pulses with 30% amplitude for 22 minutes. The lysate was centrifuged at 20.000 g at 4
307 degrees Celsius for 40 minutes, and the supernatant was collected. Filtered supernatant was
308 applied to a Ni-NTA column on a fast protein liquid chromatography system (FPLC). Eluted
309 protein fractions were analyzed by SDS-Page, pooled together and the hexahistidine-tag
310 cleaved using thrombin. After cleavage, the solution was applied to a Ni-NTA column on a fast
311 protein liquid chromatography system and the flow through collected. Suitable fractions were

312 identified by characteristic UV absorbance at 280 nm, concentrated and applied on a Superdex
313 75 16/60 column for size-exclusion chromatography. Respective fractions were pooled
314 together, concentrated to a final DARPin D1 concentration of ~25 mg/mL using a 3 kDa cutoff
315 concentrator, flash-frozen in liquid nitrogen in 50 µL aliquots, and stored at -80 degrees Celsius.
316 The concentration was determined in mg/mL using a Nanodrop- 1000 instrument against the
317 size exclusion buffer using an extinction coefficient of 0.416 $Lg^{-1}$ $cm^{-1}$.
318 To extract the active and non-aggregated tubulin from the delivered sample stocks, a sequence
319 of solution-based tubulin polymerization and depolymerization steps was performed. On ice,
320 the lyophilized tubulin is dissolved and diluted to 10 mg/mL with a polymerization buffer
321 containing 50 mM 2-(*N*-morpholino)ethanesulfonic acid (MES-KOH) pH 6.8, 0.5 mM ethylene
322 glycol-bis(β-aminoethyl ether)-N,N,N′,N′-tetraacetic acid (EGTA), 0.4 mM Guanosine-5'-
323 triphosphate (GTP), 6 mM $MgCl_2$, and 33% glycerol. The lyophilized pellet was dissolved over
324 ~30 minutes by regular shaking and pipette resuspension on ice. Afterward, the clear solution
325 was ultracentrifuged at 150.000 g at 4 degree Celsius for 10 minutes. The supernatant was
326 carefully extracted, transferred to pre-warmed tubes, and incubated for 25 minutes in a water-
327 filled heating block at 37 degree Celsius. This procedure induces tubulin polymerization
328 causing the solution to turn viscous and turbid. The solution was then ultracentrifuged at
329 300.000 g at 30 degree Celsius for 15 minutes. The supernatant was carefully discarded, and
330 the tubulin pellet was poured over with depolymerization buffer containing 80 mM Pipes-KOH
331 pH 6.8, 0.5 mM EGTA, 2 mM Guanosine-5'-diphosphate (GDP), 1 mM $MgCl_2$, and 2 mM
332 $CaCl_2$. After 15 minutes of incubation, the pellet was resuspended with a pipette, and the
333 solution was incubated again on ice for additional 15 minutes. This step was repeated until the
334 pellet was dissolved entirely. The depolymerized tubulin solution was diluted with
335 depolymerization buffer to a concentration of 9.8 mg/mL and stored at -80 degree Celsius.
336
337 **Tubulin crystallization**
338 For crystallization, the tubulin-DARPin D1 (TD1) complex was formed by mixing the
339 respective components in a 1:1.1 molar ratio. The TD1 complex was crystallized using
340 EasyXtal 15-well plates by the hanging drop vapor diffusion method (drop size 2 µL, drop ratio
341 1:1, 8 drops per well) at a concentration of 9.8 mg $mL^{-1}$ at 20°C with a precipitant solution
342 containing 21% (w/v) polyethylene glycol (PEG) 3000, 0.2 M ammonium sulfate and 0.1 M
343 bis-tris methane, pH 5.5. All drops were subsequently hair-seeded with crystalline material
344 obtained in previous crystallization trials to increase homogeneity and density of crystals. After
345 48 hours, crystals were washed off the plates with precipitant solution, collected in 0.6 ml tubes

346 and vortexed for a few seconds. This procedure induces a batch-crystallization within the tubes
347 and a sedimented crystal pellet after 24 hours of incubation at 20°C. Initially crystals grew as
348 long needles that could be broken into smaller fragments of approximately 20x20x5 $\mu m^3$ during
349 the sample preparation described below.
350
351 **Azo-CA4 synthesis**
352 The synthetic photoswitch azo-CA4 was prepared following the experimental procedure
353 described in detail by Borowiak *et al* [3]. First, catechol (4.44 g, 40.3 mmol) was reacted with
354 tosylchloride (9.53 g, 50 mmol) in pyridine (10 mL) for 2 hours at room temperature. The
355 reaction was quenched with aq HCl, and the organic phases extracted with dichloromethane,
356 dried on $MgSO_4$, filtered, concentrated and purified by column chromatography (gradient of
357 cyclohexane/EtOAc, with EtOAc from 10% to 50%), resulting in the mono-tosylated product
358 (7.5 g, 28.4 mmol) in 70% yield. Mono-tosylcatechol was then reacted with commercial 3,4,5-
359 trimethoxyanline via a diazo coupling with isopentyl nitrite. The aniline (297 mg, 1.62 mmol)
360 was dissolved in methanol (8.1 mL) and concentrated HCl (0.4 mL), and the mixture was cooled
361 in an ice bath. A solution of isopentyl nitrite (0.22 mL, 1.65 mmol) in methanol (0.97 mL) was
362 added dropwise and the reaction stirred for 30 minutes in the cold. A cold solution of the mono-
363 tosylcathecol (450 mg, 1.7 mmol) in methanol (3.2 mL) and NaOH (2.0 M, 2.9 mL) was
364 prepared, and to it was added the solution of the diazonium dropwise over 1 minute. After 5
365 hours stirring in the cold, the pH was adjusted to 7 with phosphate buffer, dichloromethane was
366 added, and the aqueous phase was extracted with dichloromethane. The combined organic
367 layers were washed with water and brine, dried on $MgSO_4$, filtered, concentrated and purified
368 by column chromatography (gradient of cyclohexane/EtOAc, with EtOAc from 20% to 50%),
369 affording the para-phenolic azobenzene (492 mg, 1.07 mmol) in 66% yield. The resulting
370 diazocompound (480 mg, 1.05 mmol) was then methylated in acetone (9.6 mL) with $K_2CO_3$
371 (431 mg, 3.12 mmol) and MeI (0,13 mL, 2.12 mmol) at room temperature for 16 hours. The
372 crude was concentrated and purified by column chromatography (cyclohexane/EtOAc, with
373 EtoAc from 10% to 50%) affording the methylated diazocompound (491 mg, 1,04 mmol) in
374 99% yield. The resulting compound (415 mg, 0.88 mmol) was then treated in basic media (KOH
375 in MeOH, reflux for 1 hour) to remove the tosyl group. The reaction mixture was concentrated,
376 dissolved in EtOAc and aq $KH_2PO_4$ (10%), the organic phases extracted with EtOAc,
377 combined, washed with water and brine and dried on $MgSO_4$. Purification by column
378 chromatography (cyclohexane/EtOAc, with EtOAc from 20% to 50%) delivered azo-CA4 (220
379 mg, 0.69 mmol) with 78% yield. Comparison to published NMR spectra[3] confirmed successful

380 synthesis (1H NMR (400 MHz, DMSO-d6) δ 9.47 (s, 1H), 7.46 (dd, J = 8.5, 2.4 Hz, 1H), 7.32
381 (d, J = 2.4 Hz, 1H), 7.18 (s, 2H), 7.12 (d, J = 8.6 Hz, 1H), 3.88 (s, 6H), 3.87 (s, 3H), 3.75 (s,
382 3H)).
383
384 **Sample preparation for serial crystallography**
385 Crystal pellets were resuspended and the contents of two 0.6 mL tubes were combined and
386 collected into 2 mL tubes. After centrifugation in a tabletop centrifuge (1000 g, 15 seconds), a
387 concentrated crystal pellet of 45-60 µL volume was obtained. The pellets were extracted,
388 transferred into PCR tubes and mixed with the *trans*-azo-CA4 to a final concentration of 1 mM.
389 To switch the compound into the binding *cis* conformation, the tubes were then illuminated for
390 at least 4 hours at 385 nm before incorporation into hydroxyethylcellulose hydrogel (Sigma-
391 Aldrich)[46]. Hydrogels containing 22% (w/v) hydroxyethylcellulose were prepared in syringes
392 and left to cure for 5 days. Illuminated crystals were transferred into a Hamilton syringe and
393 mixed into hydrogel matrix at a ratio of 4:7 using a three-way-coupler[47] before loading into the
394 high viscosity injector.
395
396 **Experimental setup and XFEL data collection**
397 Time-resolved serial crystallographic data of light-induced azo-CA4 from tubulin were
398 collected within 2 days of beamtime in September 2020 at the Alvra experimental station of
399 SwissFEL. The X-ray source provided pulses with a photon energy of 12.1 keV and a pulse
400 energy between 300 µJ and 550 µJ at a repetition rate of 100 Hz. To reduce X-ray scattering
401 (background level), the sample chamber was pumped down to a pressure of 150 mbar and then
402 refilled with helium to 500 mbar. This process was continuously repeated during the
403 measurement. Data were collected using a Jungfrau 16M operated in 4M mode. Hit rate
404 determination and initial data processing during the experiment were done with the online data
405 analysis pipeline described by Nass et al.[48].
406 TD1 crystals homogeneously incorporated into hydroxyethylcellulose were loaded into a high
407 viscosity injector connected to an HPLC pump[49]. The system extruded the crystal loaded
408 hydrogel matrix into the pump–probe interaction point through a 75 µm capillary at a flow rate
409 of 5.3 µl per minute. In the interaction point, the probing X-ray pulses intersected with a
410 circularly polarized pump beam originating from an optical parametric amplifier producing
411 laser pulses with 350 fs duration ($1/e^2$), 475 nm wavelength and 10 µJ total energy in a focal
412 spot of 65 µm ($1/e^2$) diameter; corresponding to a maximal laser fluence of 301 $mJ/cm^2$ and
413 laser power density of 861 $GW/cm^2$. In order to follow the reaction of light-induced azo-CA4

414 ligand release from tubulin between the pump laser and the probing, XFEL pulses were chosen
415 at Δt = 1 ns, 10 ns, 100 ns, 1 µs, 10 µs, 100 µs, 1 ms and 10 ms.
416
417 **Serial synchrotron crystallography**
418 Serial synchrotron data were collected using a previously described setup[25]. Crystals embedded
419 into hydroxyethylcellulose were injected in the intersecting X-ray and laser beam paths by a
420 high viscosity injector[49] with a 75 µm diameter nozzle.
421 The jet speed was set to 0.5 mm/ms and data frames were recorded using an Eiger16M detector
422 with a frame rate of 100 Hz. The beam size was set to 20 x 5 $\mu m^2$ to cover the central part of
423 the hydroxyethylcellulose column on one axis and extrusion by one frame on the other. In this
424 way we ensured the majority of crystals were exposed, whilst minimizing similarities in
425 consecutive frames for more reliable statistics. A photon flux of around 1.5 x $10^{12}$ photons/s
426 resulted in a radiation dose of about 5 kGy per recorded detector frame when calculated with
427 RADDOSE-3D[50]. Depending on their size and orientation while traversing the beam this
428 corresponds to between 5 and maximally 100 kGy per crystal. Illumination was done using
429 light at 445 nm from a laser diode with a peak optical power of 5 mW (Roithner Lasertechnik).
430 Light intensity at the interaction region was approximately 2.5 mW in a spot size of about 100
431 x 50 $mm^2$. The illumination time was set to approximately 100 ms by adjusting the distance
432 between the laser and X-ray interaction regions.
433
434 **Data processing**
435 Indexing, integrating and merging of obtained data was performed using Crystfel version
436 0.9.1[51, 52]. In detail, the peakfinder9 algorithm was used for peak detection, xgandalf[53] was used
437 to index obtained data; and peaks were integrated using --ring-radius=2,3,6 ; partialator options
438 --model=unity, --iterations=1.0, --push-res=1.5 were used to merge selected patterns. A general
439 resolution cutoff of 1.7 Å was chosen (see Supplementary Table 1) and refinements for
440 collected dark-state and apo-state data were carried out to the full resolution range. Structural
441 refinements of time-resolved data were carried out to 2.2 Å resolution due to data degradation
442 when extrapolating data (see Supplementary Table 1). Serial synchrotron crystallography data
443 obtained at SLS showed stronger anisotropy than the data obtained at the SwissFEL. The data
444 were therefore corrected for anisotropy using the STARANISO server[54].
445
446 **Difference density maps calculation**

447 Calculations of $F_{obs}$(light) – $F_{obs}$(dark) difference maps were performed using PHENIX
448 v1.19.2[55]. In detail, the multi-scaling option was used excluding amplitudes smaller than 2 σ
449 and exclusively considering the resolution range between 6 Å and 1.7 Å. For all calculated
450 $F_{obs}$(light) – $F_{obs}$(dark) difference maps, the phases of the refined dark state were used.
451 $F_{calc}$(light) – $F_{calc}$(dark) difference maps were computed to the same resolution using the CCP4
452 suite v8.0[56].
453
454 **Pearson correlation of difference maps**
455 To compute Pearson correlations independent of individual dataset multiplicities we reduced
456 the number of patterns to match the time delay where we collected the least data (55,065
457 patterns) and calculated difference maps as stated above. These difference maps where then
458 used to calculate the Pearson correlation of integrated difference electron densities[27] around all
459 protein atoms and around the ligand and all residues lying within a 3 Å sphere around the ligand.
460 Water molecules and hydrogen atoms were excluded in the selection. The density maps were
461 integrated within a 2 Å radius around the atoms and densities below 1.5 σ were ignored. The
462 resulting Pearson correlation values where normalized to the largest correlation, displayed on
463 a gray scale and values smaller than 0.3 were omitted from the figures for clarity.
464
465 **Integration of negative density around the ligand**
466 To plot the release of azo-CA4 over time we integrated the negative density around the ligand
467 in same way as the Pearson correlation data for the whole protein (1.5 A radius, 3.0 sigma
468 cutoff). The integrated negative density was normalized: the highest value (apo) was set to 1
469 the lowest negative ligand density (1 ms) was set to 0. Since apo data and time-resolved data
470 from the XFEL experiment are not fully comparable due to a roughly 4 fold difference in
471 occupancy. The negative density of the apo state was downscaled to lower occupancy by
472 assuming a roughly 4-fold occupancy increase is similar to a 4-fold increase of the number of
473 observations, resulting in an estimated scaling factor of 0.5 (assuming signal to noise improves
474 by $\sqrt{2}$ for doubling the number of observations).
475
476 **Data extrapolation**
477 Calculation of extrapolated data was performed using the method described by Pandey et al.[29].
478 Briefly, the linear approximation was used: $F_{extra} = [100/A \times (F_{obs}(\text{light}) - F_{obs}(\text{dark})] + F_{calc}$,
479 with A representing the activation level in percent, Fcalc representing amplitudes of the high-
480 resolution dark state model and $F_{extra}$ representing the extrapolated structure factor amplitude.

481 The activation level A, defined as the percentage of dark state molecules being activated after
482 pump laser pulse exposure, was determined as described[29]. Briefly, extrapolated data were
483 calculated using a decreasing activation level A. Then the negative electron density in $2F_{extra}$-
484 $F_{calc}$ maps calculated using the dark model phases, was integrated around nitrogen atoms of the
485 ligand which have strong negative difference density peaks on them in each of the light
486 activated structures and hence leave their position. The negative density was then plotted
487 against the activation level. The intersection of the linear parts of the resulting graph (negative
488 density is zero for not enough dark state subtracted and starts to linearly increase as dark is over
489 subtracted) was taken as the activation level. The activation levels determined in this way
490 fluctuated between 18-27% but since all data were measured under the same conditions, we
491 chose the average of 22% to refine the structures. As a further control we determined the
492 activation level using the re-appearance of dark state features in $2F_{extra}$-$F_{calc}$ maps[57, 58], which
493 confirmed our initial assignment.
494
495 **Structure determination and refinement**
496 The structure of the dark-state was solved by molecular replacement with 5NQT as a search
497 model. Structural refinements of the model were done using PHENIX v1.19.2[55] with iterative
498 cycles of manual adjustments made in Coot v0.9.8.1[59]. As a final step the ligand was refined
499 using Buster v2.10.4[60], employing the -qm option to use a quantum mechanics target for the
500 ligand rather than restraints which may be a source of errors, especially for molecules which
501 are not at their energy minimum. The structure of the apo-state was directly refined using the
502 final dark-state structure as a starting point.
503 Before the actual refinement and model building of the obtained time-resolved data, the
504 negative amplitudes resulting from the extrapolation procedure were removed. The models
505 were manually adjusted to best fit observed difference map features as well as extrapolated
506 maps using the final dark-state model as a starting point.
507 Before the actual refinement and model building of the obtained time-resolved data, the
508 negative amplitudes resulting from the extrapolation procedure were removed. The models
509 were manually adjusted to best match observed difference map features, to produce similar
510 $F_{calc}$(light)-$F_{calc}$(dark) maps and to fit extrapolated maps using the final dark model as a starting
511 point. To match the observed difference density features using $F_{calc}$(1 ms)-$F_{calc}$(dark) maps we
512 chose to exclude Leu246 from XYZ refinement after manual adjustment for the 1 ms structure.
513 Given the activation level of 22 percent, we choose to refine the predominant structural species
514 by comparing the models to previous and consecutive structures.

515

516 **Binding pocket and protein backbone analysis**

517 Protein interactions in the binding pocket were identified with the protein-ligand interaction
518 profiler[61]. Changes in the volume of the colchicine-site over time were determined using
519 PyVOL[62] with the parameters (β–tubulin, minimum radius = 1.65; maximum radius = 3.8;
520 minimum volume = 50, standard partitioning).

521 To visualize global protein backbone movements, alternative conformers were removed and
522 structures truncated to poly-Ala using Phenix PDB tools[55]. Respective structural displacements
523 of secondary structural elements were indicated using the PyMOL Python script Modevectors
524 (by Sean M. Law, University of Michigan). Displacements greater than 0.5 Å were classified
525 as significant (cutoff=0.5). For visualization purposes, only the displacement vectors of every
526 second (skip=2) Cα-backbone atom (atom=CA) were shown and the vectors amplified by a
527 factor of 6 (factor=6). Additional settings involve the vector representation (head=2.0,
528 tail=0.85, head_length=3.0, cut=0).

529 To find possible release pathways during reorganization of the binding pocket we used the
530 program Caver 3.03[63] using the following settings: minimum probe radius = 1.9 Å, shell depth
531 = 4 Å, and shell radius = 5 Å, azo-CA4 position as starting coordinate.

532

533 **Time-resolved spectroscopy measurements**

534 The time-resolved transient absorption data were recorded using a home-built pump–probe
535 setup, as described in detail previously[64]. In short, the fundamental laser pulses (1 mJ, 775 nm,
536 130 fs, 1 kHz) were provided by a Ti:Sa amplifier (Clark, MXR-CPA-iSeries). The pump pulses
537 at 438 nm were generated using a home-built two stage NOPA (noncollinear optical parametric
538 amplifier) and sum frequency mixing. The pulses were pre-compressed in a prism compressor
539 located between the two NOPA stages. White light continuum pulses (300-750 nm) were
540 generated by focusing a fraction of the laser fundamental beam into a $CaF_2$-crystal (5 mm). The
541 continuum pulses were split into probe and reference beams. The reference beam was guided
542 directly into a spectrograph, while the probe beam was focused at the sample position then
543 collected and directed into a second spectrograph. The spectrographs (AMKO Multimode)
544 contained gratings with 600 grooves/mm blazed at 300 nm and a photodiode array. The
545 instrument response function (IRF) of ~100 fs in the experiments was estimated from the pump
546 probe cross correlation. Anisotropic contributions to the measurements were avoided by
547 performing the experiments at the magic angle condition (54.7° pump-probe polarization
548 difference). The samples were held in a fused silica cuvette with an optical path length of 1 mm

549 which was constantly moved in the plane perpendicular to the direction of the probe pulse
550 propagation to avoid accumulation of photoproducts. To keep the azo-CA4 samples (bound and
551 free) in the *cis* isomer state, the cuvette was continuously illuminated with a high-power LED
552 at 385 nm. Global analysis of the experimental data was performed using OPTIMUS
553 (www.optimusfit.org)[64] to recover the lifetimes describing the *cis* → *trans* photoisomerization
554 kinetics. With the help of target analysis, a sequential kinetic scheme was fitted to the
555 experimental data to obtain the times of the highest population of each kinetic state, which were
556 helpful in determining the optimal time points for the XFEL experiments.
557
558 **Computational Methods**
559 **System preparation**
560 The starting models for simulations were built from the respective XFEL-based time-resolved
561 structures. We removed the DARPin protein and reconstructed the βM-loop (res 272-288) using
562 the one in chain D of PDB 4I4T as a template by employing the Prime[65] module of the
563 Schrödinger 2020-4 suite. Analogously, $Mg^{2+}$ ion in chain B (β-tubulin) was added by
564 superimposition with the one of chain D of 4I4T structure. Calcium ions were removed from
565 the model.
566 The final model consisted of an αβ-tubulin heterodimer in complex with azo-CA4, GTP, and
567 GDP molecules bound to the α- and β-tubulin subunits, respectively, as well as their associated
568 $Mg^{2+}$ ions and their coordinating water molecules. The resulting protein structure possessed
569 437 out of 451 residues of α-tubulin (UniProtKB ID P81947) and 431 out of 445 residues of β-
570 tubulin (UniProtKB ID Q6B856). Missing residues belonging to the intrinsically disordered C-
571 terminal tails of α- and β-tubulin were not modeled and C-termini were capped with N-methyl
572 amide (NME) groups. Residue protonation states were evaluated at pH 7.0 using the Protein
573 Preparation Wizard tool[66] implemented in the Schrödinger 2020-4 suite[67]. The αβ-tubulin
574 heterodimer structure was solvated with the TIP3P-model[68] for water molecules in a truncated
575 octahedron box using 12 Å as the minimum distance between the protein and the box edges.
576 The system was neutralized by adding Na+ ions resulting in a total of about 122k atoms. The
577 atomistic force field Amber-ff14SB[69] was used for all simulations. Parameters for $Mg^{2+}$ ions
578 and the GTP and GDP molecules were developed by Allner et al.[70] and Meagher et al.[71],
579 respectively.
580 Concerning the ligand, partial atomic charges were obtained with the Restrained Electrostatic
581 Potential (RESP) method on a DFT-optimized trans conformation at the B3LYP/6-31g* level.
582 The geometric optimization was carried out with Terachem v1.94. The General Amber

583 ForceField (GAFF) was used, with custom parameters for the three main dihedral angles: 1-1a-
584 1b-1', 6-1-1a-1b, 1a-1b-1'-6'.
585 To obtain such optimized parameters, we fitted the GAFF energy curves associated with a rigid
586 torsion of the dihedral angles to the corresponding DFT energy curves. For each dihedral, we
587 proceeded as follows: we started out with the geometrically optimized *trans* structure. We then
588 performed a clockwise rigid rotation with 15° steps followed by an analogous counter-
589 clockwise rigid rotation. For each rotation step we performed a DFT geometric optimization
590 restraining the rotated dihedral, and we evaluated the energy. We retained the minimum energy
591 among the clockwise and anticlockwise rotation cycles to overcome hysteresis. The three
592 resulting DFT energy profiles consisting of 24 evaluation points were used as a target for the
593 fitting procedure. DFT calculations were performed with Terachem v1.94, at the B3LYP/6-
594 31g* level. The fitting procedure was carried out separately for the three energy profiles with
595 mdgx, part of AmberTools21. The αβ-tubulin heterodimer system was assembled with the
596 LEaP tool implemented in the AmberTools 21 software package[67].
597 The designed models for QM calculations consisted of protein residues α(99-101, 178-181),
598 β(237-242, 248-259, 314-321, 349-354, 378-380), with the respective N- and C- termini capped
599 with acetyl (ACE) and NME groups, the azo-CA4 molecule, and its two closest water
600 molecules. They resulted in 743 atoms.
601
602 **Molecular dynamics simulations**
603 Plain molecular dynamics simulations starting from the tubulin-trans-azo-CA4-tubulin
604 complex 1 ms structure were performed using the Amber20 engine[67]. The system, after a
605 preliminary stage of energy minimization (1000 steps of steepest descent and 9000 of conjugate
606 gradient), was heated to the target temperature of 300 K with a 250 ps ramp using an integration
607 time-step of 1 ps and the weak-coupling algorithm, followed by another 500 ps of simulation
608 in the NVT ensemble after switching to an integration time-step of 2 ps. Subsequently, in order
609 to the equilibrate box dimensions, the system was simulated for 1 ns in the NPT ensemble using
610 the Berendsen barostat. For these initial stages, heavy atoms were harmonically restrained with
611 a force constant of 5 kcal/mol/Å$^2$. Finally, a last stage of 5 ns in the NVT ensemble, using the
612 Langevin thermostat with a collision frequency g of 2.0 ps-1. Bonds involving hydrogen atoms
613 were restrained, and a short-range, non-bonded cut-off of 8 Å was applied, whereas long-range
614 electrostatics were treated with the particle mesh Ewald (PME) method[72]. Periodic boundary
615 conditions (PBC) were applied.

616 After the equilibration stage, a cumulative 30 μs-long MD simulation was conducted with an
617 integration time step of 2 fs in the NVT ensemble at a target temperature of 300 K.
618 In order to evaluate the $\Delta\Delta G_{cis\text{-}trans}$, well-tempered metadynamics (WTMD) simulations[73] were
619 performed with GROMACS 2020.2[74] and PLUMED 2.6.1[75]. We performed WTMD enhancing
620 the sampling of the two dihedral angles 1-1a-1b-1' and 6-1-1a-1b for both the bound and the
621 unbound state. The bias factor, the deposition rate, the initial hill height, and the hill width were
622 set to 45, 0.5 ps−1, 2.5 kJ·mol−1, and 0.3 rad, respectively.
623 The WTMD simulation of the bound state was carefully designed to sample conformations
624 compatible with the XFEL-based time-resolved structures. A positional harmonic restraint with
625 K=100 kJ/mol $nm^2$ was introduced on the backbone of the protein together with the supervision
626 of the hydrogen bond to the backbone carbonyl of αThr179. With this regard, the simulation
627 was stopped and restarted with regenerated velocities whenever the H-bond was broken. The
628 resulting trajectory of 400 ns was reweighted in order to reconstruct the free energy profile.
629 Block analysis with a block size of 50 ns was performed to assess convergence and to plot 95%
630 confidence interval error bands. We performed WTMD enhancing the sampling of the two
631 dihedral angles 1-1a-1b-1' and 6-1-1a-1b. The bias factor, the deposition rate, the initial hill
632 height, and the hill width were set to 45, 0.5 ps−1, 2.5 kJ·mol−1 740, and 0.3 rad, respectively.
633 The WTMD simulation of the unbound state was performed with the same parameters used for
634 the bound state. In this case, we simulated a single ligand molecule in a solvated cubic box
635 using 10 Å as the minimum distance between the ligand and the box edges. After standard
636 minimization, thermalization and equilibration phases WTMD was carried out for 400 ns. The
637 resulting trajectory was reweighted in order to reconstruct the free energy profile. Block
638 analysis with block size of 50 ns was performed to assess convergence and to plot 95%
639 confidence interval error bands.
640
641 **Data availability**
642 The pdb entry 4I4T [http://doi.org/10.2210/pdb4I4T/pdb] (tubulin-RB-TTL complex) was used
643 as starting point to prepare the QM simulations. For molecular replacement we used pdb entry
644 5NQT [http://doi.org/10.2210/pdb5NQT/pdb] (tubulin-darpin complex). We used the pbd entry
645 5SYE [http://doi.org/10.2210/pdb5SYE/pdb] (taxol-stabilized microtubule) to represent the
646 tubulin conformation found in microtubules. Coordinates and structure factors of the presented
647 serial femtosecond crystallographic structures have been deposited in the PDB database under
648 accession code 7YYQ [http://doi.org/10.2210/pdb7YYQ/pdb] (dark) and 7YZ3
649 [http://doi.org/10.2210/pdb7YZ3/pdb] (apo). The serial synchrotron data have been deposited

650 under 7YZ6 [http://doi.org/10.2210/pdb7YZ6/pdb] (dark) and 7YZ5
651 [http://doi.org/10.2210/pdb7YZ5/pdb] (100 ms). Models refined against extrapolated data,
652 extrapolated structure factors and light data used for data extrapolation have been deposited
653 under accession codes 7YYV [http://doi.org/10.2210/pdb7YYV/pdb] (1 ns), 7YYW
654 [http://doi.org/10.2210/pdb7YYW/pdb] (10 ns), 7YYX
655 [http://doi.org/10.2210/pdb7YYX/pdb] (100 ns), 7YYY
656 [http://doi.org/10.2210/pdb7YYY/pdb] (1 µs), 7YYZ [http://doi.org/10.2210/pdb7YYZ/pdb]
657 (10 µs), 7YZ0 [http://doi.org/10.2210/pdb7YZ0/pdb] (100 µs), 7YZ1
658 [http://doi.org/10.2210/pdb7YZ1/pdb] (1 ms) and 7YZ2 [http://doi.org/10.2210/pdb7YZ2/pdb]
659 (10 ms). The start and end coordinates of the molecular dynamics simulations are provided as
660 Source Data file.
661

662 **References:**


663 1. Hull K, Morstein J, Trauner D. In Vivo Photopharmacology. *Chem Rev* **118**, 10710-
664 10747 (2018).
665
666 2. Beharry AA, Woolley GA. Azobenzene photoswitches for biomolecules. *Chem Soc*
667 *Rev* **40**, 4422-4437 (2011).
668
669 3. Borowiak M*, et al.* Photoswitchable Inhibitors of Microtubule Dynamics Optically
670 Control Mitosis and Cell Death. *Cell* **162**, 403-411 (2015).
671
672 4. Gaspari R, Prota AE, Bargsten K, Cavalli A, Steinmetz MO. Structural Basis of cis-
673 and trans-Combretastatin Binding to Tubulin. *Chem-Us* **2**, 102-113 (2017).
674
675 5. Brouhard GJ, Rice LM. Microtubule dynamics: an interplay of biochemistry and
676 mechanics. *Nat Rev Mol Cell Biol* **19**, 451-463 (2018).
677
678 6. Dalbeth N, Lauterio TJ, Wolfe HR. Mechanism of action of colchicine in the
679 treatment of gout. *Clin Ther* **36**, 1465-1479 (2014).
680
681 7. Pettit GR, Singh SB, Hamel E, Lin CM, Alberts DS, Garcia-Kendall D. Isolation and
682 structure of the strong cell growth and tubulin inhibitor combretastatin A-4.
683 *Experientia* **45**, 209-211 (1989).
684
685 8. Grisham R, Ky B, Tewari KS, Chaplin DJ, Walker J. Clinical trial experience with
686 CA4P anticancer therapy: focus on efficacy, cardiovascular adverse events, and
687 hypertension management. *Gynecol Oncol Res Pract* **5**, 1 (2018).
688
689 9. Baytas SN. Recent Advances in Combretastatin A-4 Inspired Inhibitors of Tubulin
690 Polymerization: An Update. *Curr Med Chem* **29**, 3557-3585 (2022).
691
692 10. Barnette KG*, et al.* Oral Sabizabulin for High-Risk, Hospitalized Adults with Covid-
693 19: Interim Analysis. *NEJM Evidence* **0**, EVIDoa2200145 (2022).
694

11. Jerca FA, Jerca VV, Hoogenboom R. Advances and opportunities in the exciting world of azobenzenes. *Nature Reviews Chemistry* **6**, 51-69 (2022).

12. Bozovic O, Jankovic B, Hamm P. Using azobenzene photocontrol to set proteins in motion. *Nature Reviews Chemistry* **6**, 112-124 (2022).

13. Neutze R, Moffat K. Time-resolved structural studies at synchrotrons and X-ray free electron lasers: opportunities and challenges. *Curr Opin Struc Biol* **22**, 651-659 (2012).

14. Tenboer J*, et al.* Time-resolved serial crystallography captures high-resolution intermediates of photoactive yellow protein. *Science* **346**, 1242-1246 (2014).

15. Monteiro DCF, Amoah E, Rogers C, Pearson AR. Using photocaging for fast time-resolved structural biology studies. *Acta Crystallographica Section D* **77**, (2021).

16. Steinmetz MO, Prota AE. Microtubule-Targeting Agents: Strategies To Hijack the Cytoskeleton. *Trends Cell Biol* **28**, 776-792 (2018).

17. Branden G, Neutze R. Advances and challenges in time-resolved macromolecular crystallography. *Science* **373**, 980-+ (2021).

18. Orville AM. Recent results in time resolved serial femtosecond crystallography at XFELs. *Curr Opin Struc Biol* **65**, 193-208 (2020).

19. Gao L*, et al.* A Robust, GFP-Orthogonal Photoswitchable Inhibitor Scaffold Extends Optical Control over the Microtubule Cytoskeleton. *Cell Chem Biol* **28**, 228-241 e226 (2021).

20. Gao L*, et al.* In Vivo Photocontrol of Microtubule Dynamics and Integrity, Migration and Mitosis, by the Potent GFP-Imaging-Compatible Photoswitchable Reagents SBTubA4P and SBTub2M. *J Am Chem Soc* **144**, 5614-5628 (2022).

21. Kirchner S, Pianowski Z. Photopharmacology of Antimitotic Agents. *Int J Mol Sci* **23**, (2022).

22. Pecqueur L*, et al.* A designed ankyrin repeat protein selected to bind to tubulin caps the microtubule plus end. *Proc Natl Acad Sci U S A* **109**, 12011-12016 (2012).

23. La Sala G*, et al.* Structure, Thermodynamics, and Kinetics of Plinabulin Binding to Two Tubulin Isotypes. *Chem-Us* **5**, 2969-2986 (2019).

24. Weinert T*, et al.* Serial millisecond crystallography for routine room-temperature structure determination at synchrotrons. *Nat Commun* **8**, 542 (2017).

25. Weinert T*, et al.* Proton uptake mechanism in bacteriorhodopsin captured by serial synchrotron crystallography. *Science* **365**, 61-65 (2019).

26. Abela R*, et al.* Perspective: Opportunities for ultrafast science at SwissFEL. *Struct Dyn* **4**, 061602 (2017).

27. Wickstrand C, *et al.* A tool for visualizing protein motions in time-resolved crystallography. *Struct Dyn* **7**, 024701 (2020).

28. Skopintsev P, *et al.* Femtosecond-to-millisecond structural changes in a light-driven sodium pump. *Nature*, (2020).

29. Pandey S, *et al.* Time-resolved serial femtosecond crystallography at the European XFEL. *Nature Methods* **17**, 73-+ (2020).

30. Decherchi S, Cavalli A. Thermodynamics and Kinetics of Drug-Target Binding by Molecular Simulation. *Chem Rev* **120**, 12788-12833 (2020).

31. Prota AE, *et al.* The Novel Microtubule-Destabilizing Drug BAL27862 Binds to the Colchicine Site of Tubulin with Distinct Effects on Microtubule Organization. *Journal of Molecular Biology* **426**, 1848-1860 (2014).

32. Dorleans A, Gigant B, Ravelli RBG, Mailliet P, Mikol V, Knossow M. Variations in the colchicine-binding domain provide insight into the structural switch of tubulin. *P Natl Acad Sci USA* **106**, 13775-13779 (2009).

33. Ravelli RBG, *et al.* Insight into tubulin regulation from a complex with colchicine and a stathmin-like domain. *Nature* **428**, 198-202 (2004).

34. Muhlethaler T, Gioia D, Prota AE, Sharpe ME, Cavalli A, Steinmetz MO. Comprehensive Analysis of Binding Sites in Tubulin. *Angew Chem Int Ed Engl* **60**, 13331-13342 (2021).

35. Knossow M, Campanacci V, Khodja LA, Gigant B. The Mechanism of Tubulin Assembly into Microtubules: Insights from Structural Studies. *iScience* **23**, 101511 (2020).

36. Brouhard GJ, Rice LM. The contribution of alphabeta-tubulin curvature to microtubule dynamics. *J Cell Biol* **207**, 323-334 (2014).

37. Gaillard N, *et al.* Inhibiting parasite proliferation using a rationally designed anti-tubulin agent. *Embo Mol Med* **13**, (2021).

38. Mehrabi P, *et al.* Time-resolved crystallography reveals allosteric communication aligned with molecular breathing. *Science* **365**, 1167-1170 (2019).

39. Pandey S, *et al.* Observation of substrate diffusion and ligand binding in enzyme crystals using high-repetition-rate mix-and-inject serial crystallography. *Iucrj* **8**, 878-895 (2021).

40. Butryn A, *et al.* An on-demand, drop-on-drop method for studying enzyme catalysis by serial crystallography. *Nat Commun* **12**, 4461 (2021).

41. Schmidt M. Reaction Initiation in Enzyme Crystals by Diffusion of Substrate. *Crystals* **10**, (2020).

42. Ricart-Ortega M, Font J, Llebaria A. GPCR photopharmacology. *Mol Cell Endocrinol* **488**, 36-51 (2019).

43. Velema WA, Szymanski W, Feringa BL. Photopharmacology: beyond proof of principle. *J Am Chem Soc* **136**, 2178-2191 (2014).

44. Leippe P, Frank JA. Designing azobenzene-based tools for controlling neurotransmission. *Curr Opin Struct Biol* **57**, 23-30 (2019).

45. Muhlethaler T*, et al.* Crystallization Systems for the High-Resolution Structural Analysis of Tubulin-Ligand Complexes. *Methods Mol Biol* **2430**, 349-374 (2022).

46. Sugahara M*, et al.* Hydroxyethyl cellulose matrix applied to serial crystallography. *Sci Rep* **7**, 703 (2017).

47. James D*, et al.* Improving High Viscosity Extrusion of Microcrystals for Time-resolved Serial Femtosecond Crystallography at X-ray Lasers. *J Vis Exp*, (2019).

48. Nass K*, et al.* Pink-beam serial femtosecond crystallography for accurate structure-factor determination at an X-ray free-electron laser. *IUCrJ* **8**, (2021).

49. Weierstall U*, et al.* Lipidic cubic phase injector facilitates membrane protein serial femtosecond crystallography. *Nat Commun* **5**, 3309 (2014).

50. Zeldin OB, Gerstel M, Garman EF. RADDOSE-3D: time- and space-resolved modelling of dose in macromolecular crystallography. *Journal of Applied Crystallography* **46**, 1225-1230 (2013).

51. White TA*, et al.* CrystFEL: a software suite for snapshot serial crystallography. *Journal of Applied Crystallography* **45**, 335-341 (2012).

52. White TA*, et al.* Recent developments in CrystFEL. *J Appl Crystallogr* **49**, 680-689 (2016).

53. Gevorkov Y*, et al.* XGANDALF - extended gradient descent algorithm for lattice finding. *Acta Crystallogr A Found Adv* **75**, 694-704 (2019).

54. Tickle IJ, Flensburg, C., Keller, P., Paciorek, W., Sharff, A., Vonrhein, C., Bricogne, G. . STARANISO.). Cambridge, United Kingdom: Global Phasing Ltd. (2018).

55. Adams PD*, et al.* PHENIX: building new software for automated crystallographic structure determination. *Acta Crystallogr D Biol Crystallogr* **58**, 1948-1954 (2002).

56. Winn MD*, et al.* Overview of the CCP4 suite and current developments. *Acta Crystallogr D Biol Crystallogr* **67**, 235-242 (2011).

57. Gorel A, Schlichting I, Barends TRM. Discerning best practices in XFEL-based biological crystallography - standards for nonstandard experiments. *Iucrj* **8**, 532-543 (2021).

58. Nogly P*, et al.* Retinal isomerization in bacteriorhodopsin captured by a femtosecond x-ray laser. *Science* **361**, (2018).

59. Emsley P, Cowtan K. Coot: model-building tools for molecular graphics. *Acta Crystallogr D Biol Crystallogr* **60**, 2126-2132 (2004).

60. Bricogne G BE, Brandl M, Flensburg C, Keller P, Paciorek W, Roversi P, Sharff A, Smart O, Vonrhein C, Womack T BUSTER version 2.10.4.). Cambridge, United Kingdom: Global Phasing Ltd. (2021).

61. Salentin S, Schreiber S, Haupt VJ, Adasme MF, Schroeder M. PLIP: fully automated protein-ligand interaction profiler. *Nucleic Acids Res* **43**, W443-447 (2015).

62. Smith RHB, Dar AC, Schlessinger A. PyVOL: a PyMOL plugin for visualization, comparison, and volume calculation of drug-binding sites. *bioRxiv*, 816702 (2019).

63. Chovancova E*, et al.* CAVER 3.0: a tool for the analysis of transport pathways in dynamic protein structures. *PLoS Comput Biol* **8**, e1002708 (2012).

64. Slavov C*, et al.* The ultrafast reactions in the photochromic cycle of water-soluble fulgimide photoswitches. *Phys Chem Chem Phys* **18**, 10289-10296 (2016).

65. Jacobson MP, Friesner RA, Xiang Z, Honig B. On the role of the crystal environment in determining protein side-chain conformations. *J Mol Biol* **320**, 597-608 (2002).

66. Sastry GM, Adzhigirey M, Day T, Annabhimoju R, Sherman W. Protein and ligand preparation: parameters, protocols, and influence on virtual screening enrichments. *J Comput Aided Mol Des* **27**, 221-234 (2013).

67. D.A. Case HMA, K. Belfon, I.Y. Ben-Shalom, S.R. Brozell, D.S. Cerutti, T.E. Cheatham, III, G.A. Cisneros, V.W.D. Cruzeiro, T.A. Darden, R.E. Duke, G. Giambasu, M.K. Gilson, H. Gohlke, A.W. Goetz, R. Harris, S. Izadi, S.A. Izmailov, C. Jin, K. Kasavajhala, M.C. Kaymak, E. King, A. Kovalenko, T. Kurtzman, T.S. Lee, S. LeGrand, P. Li, C. Lin, J. Liu, T. Luchko, R. Luo, M. Machado, V. Man, M. Manathunga, K.M. Merz, Y. Miao, O. Mikhailovskii, G. Monard, H. Nguyen, K.A. O'Hearn, A. Onufriev, F. Pan, S. Pantano, R. Qi, A. Rahnamoun, D.R. Roe, A. Roitberg, C. Sagui, S. Schott-Verdugo, J. Shen, C.L. Simmerling, N.R. Skrynnikov, J. Smith, J. Swails, R.C. Walker, J. Wang, H. Wei, R.M. Wolf, X. Wu, Y. Xue, D.M. York, S. Zhao, and P.A. Kollman. Amber 21. In: *University of California, San Francisco*) (2021).

68. Jorgensen WL, Chandrasekhar J, Madura JD, Impey RW, Klein ML. Comparison of Simple Potential Functions for Simulating Liquid Water. *J Chem Phys* **79**, 926-935 (1983).

69. Maier JA, Martinez C, Kasavajhala K, Wickstrom L, Hauser KE, Simmerling C. ff14SB: Improving the Accuracy of Protein Side Chain and Backbone Parameters from ff99SB. *J Chem Theory Comput* **11**, 3696-3713 (2015).

70. Allner O, Nilsson L, Villa A. Magnesium Ion-Water Coordination and Exchange in Biomolecular Simulations. *J Chem Theory Comput* **8**, 1493-1502 (2012).

71. Meagher KL, Redman LT, Carlson HA. Development of polyphosphate parameters for use with the AMBER force field. *J Comput Chem* **24**, 1016-1025 (2003).

72. Salomon-Ferrer R, Gotz AW, Poole D, Le Grand S, Walker RC. Routine Microsecond Molecular Dynamics Simulations with AMBER on GPUs. 2. Explicit Solvent Particle Mesh Ewald. *Journal of Chemical Theory and Computation* **9**, 3878-3888 (2013).

73. Barducci A, Bussi G, Parrinello M. Well-tempered metadynamics: A smoothly converging and tunable free-energy method. *Phys Rev Lett* **100**, (2008).

74. Van der Spoel D, Lindahl E, Hess B, Groenhof G, Mark AE, Berendsen HJC. GROMACS: Fast, flexible, and free. *J Comput Chem* **26**, 1701-1718 (2005).

75. Tribello GA, Bonomi M, Branduardi D, Camilloni C, Bussi G. PLUMED 2: New feathers for an old bird. *Comput Phys Commun* **185**, 604-613 (2014).

## Acknowledgments

We are grateful for the excellent support from the PSI Crystallization Facility and the Macromolecular Crystallography group during growing and testing of crystals at the Swiss Light Source. The Biomolecular Structure and Mechanism Program of the Life Science Zürich Graduate School is acknowledged for their academic framework for our graduate students. This project was founded by the following agencies: The Swiss National Science Foundation project grants 31003A_179351 (to J.S.), to 310030_197674 (to T.W.), 310030_192566 (to M.O.S.) and the NCCR:MUST (to C.M. and J.S.), the Swiss Nanoscience Institute SNI #1904 (to M.C.), Deutsche Forschungsgemeinschaft, Project WA 1850/4-3 (C.S. and J.W.).

## Author contributions

The project was coordinated and led by J.S. following input on time-resolved serial crystallographic data acquisition and evaluation from T.W., computer simulations from A.C., and time-resolved spectroscopy from J.W. and tubulin structural biology from M.O.S.. The TD1 protein complex was purified and crystallized by M.Wr. with the help from A.F., N.G., and other members of the team during the large-scale preparation phase. The azo-CA4 compound was synthesized by T.Ma.. Crystal injection was optimized by M.Wr., A.F., and D.J.. The lipidic cubic phase injector was operated and aligned during the beamtime by A.F. D.Ga., and D.J.. The endstation including the laser system were aligned and operated by P.J.M.J., D.O., K.N., C.C., J.B., C.B. and C.M. Sample preparation during the beamtime was done by M.Wr., A.F., M.C., R.S., D.K. and H.G.. Data processing during the beamtime was initially done using the online data analysis pipeline established by K.N. and D.O. followed by

manual optimization by S.B. and P.S. with instructions from T.W.. The synchrotron setup was aligned and optimized by F.D., D.J. and W.Wa..

Final structures were refined by M.Wr. and T.W. and interpreted together with J.S.. Quantum chemical calculations were done by M.F. and D.Gi. under supervision of A.C.. The time-resolved spectroscopic experiments were done by N.G., T.W., and C.S. and interpreted together with M.B. and J.W.. The manuscript was written by T.W., M.Wr., M.O.S. and J.S. with further suggestions from the other authors.

**Competing interest declaration**

The authors declare that they have no competing interests.

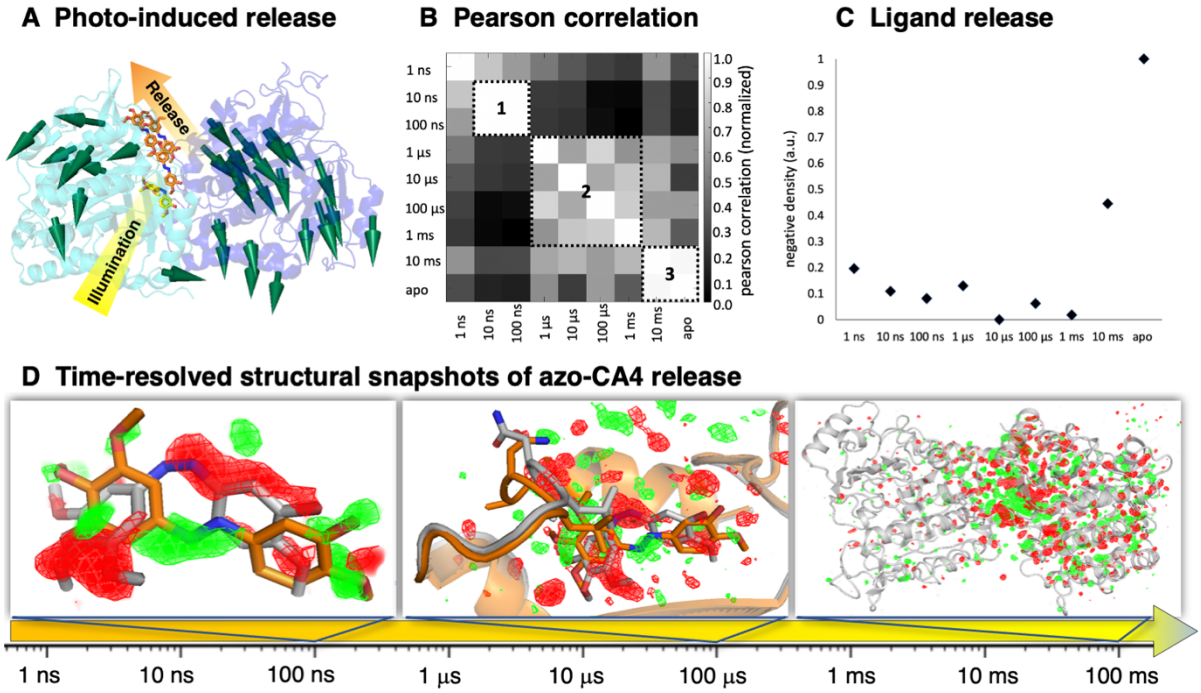


**Figure 1: Tracking ligand release from tubulin using a photochemical affinity switch.** (**A**) The cis-azo-CA4 (yellow sticks) binds to the colchicine site that is formed by secondary structural elements stemming from both the α (blue) and β (cyan) subunits of the αβ-tubulin heterodimer. Illumination with a flash of a laser light triggers the release of *trans*-azo-CA4 (colored in orange, diffusion indicated by including several molecules, cylindrical arrows designate conformational changes of the protein) from its binding pocket. (**B**) Difference electron density maps ($F_{obs}$(light)-$F_{obs}$(dark)) from time-resolved XFEL data were integrated and subjected to Pearson correlation analysis. Three areas of elevated correlation can be identified. The box in the nanoseconds (**1**) corresponds to the relaxed conformation of the ligand observed as a metastable binding pose. Correlations between maps in the microseconds (**2**) are less homogeneous and stretch from 1 µs to opening of the exit pathway at 1 ms. The final snapshots in the milliseconds (**3**) corresponds to the predominantly unliganded protein. (**C**) Plot showing negative density integrated around azo-CA4 with a strong increase after 1 ms indicating release of the ligand. (**D**) Time-resolved structural snapshots of azo-CA4 release. The time arrow depicts the investigated time regime. The panels show from left to right the isomorphous difference maps obtained at 100 ns with changes centered on the ligand, 100 µs with changes centered on the binding pocket, and 100 ms with conformational changes propagating throughout the protein. All panels show isomorphous difference maps in red (negative) and green (positive) at 3 σ. The structure in the given time range (colored in orange) is compared to that of the previous time range (colored in grey). A movie showing the electron changes within the binding pocket over all nine time delays is available as supplementary material.

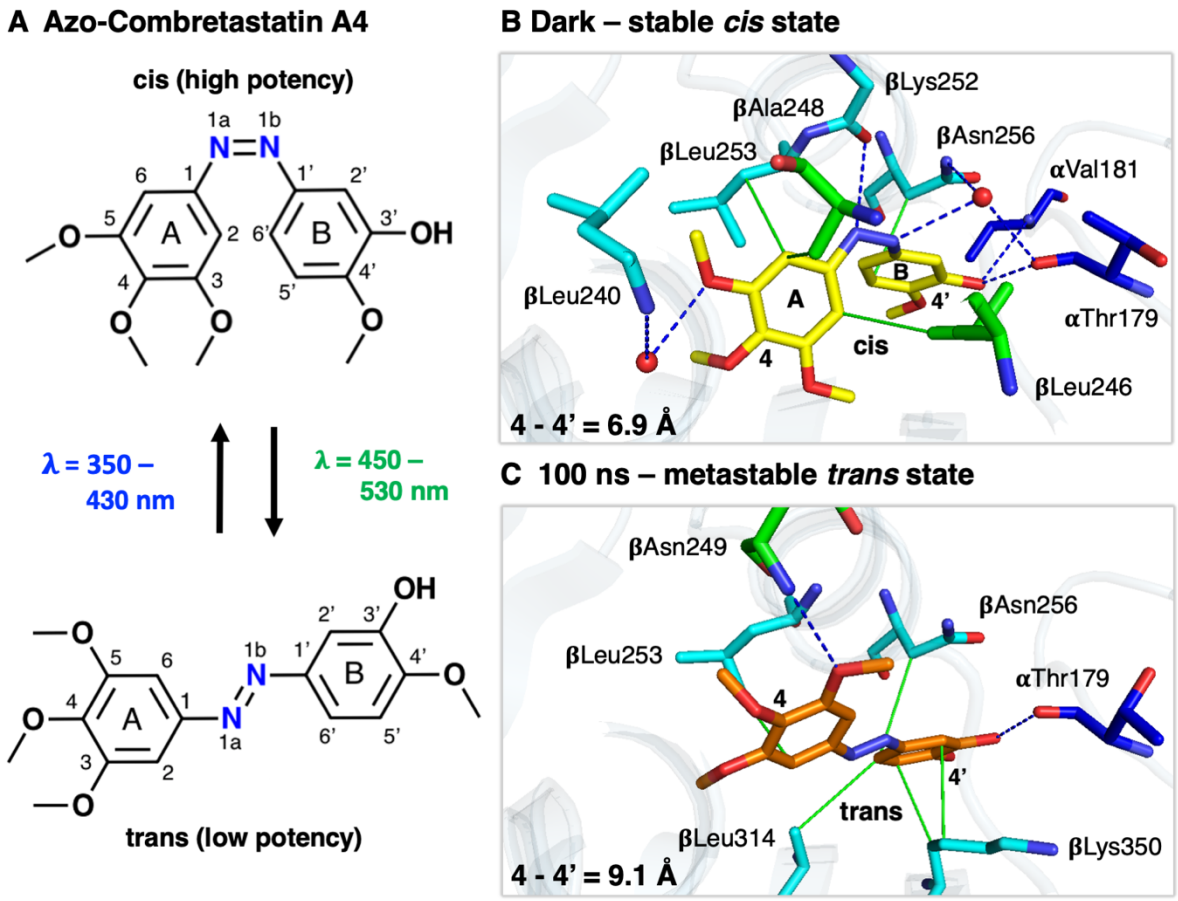


**Figure 2: Photoisomerization leads to the formation of a metastable binding state. (A)** The two chemical structures of azo-CA4 show the wavelength dependent conformational change between the *cis* (top) and *trans* (bottom) positions. Central to the switch is the N=N azo bond that allows to switch azo-CA4 reversibly and with high efficiency between its high and low affinity stereoisomers, respectively. (**B**) Before laser induced isomerization, *cis*-azo-CA4 (yellow sticks) is bound in the colchicine-site located between the α (blue) and β (cyan) subunits close to the βT7 loop (green) of β-tubulin. Hydrophobic interactions (green lines) between tubulin residues and the A and B rings of *cis*-azo-CA4 as well as hydrophilic interactions (blue dashed lines) towards the ring substituents anchor the ligand within the colchicine- site. (**C**) Within nanoseconds after illumination, *trans*-azo-CA4 (orange sticks) has relaxed into a metastable binding pose with altered interaction network and reduced affinity. For clarity only interacting residues are shown.

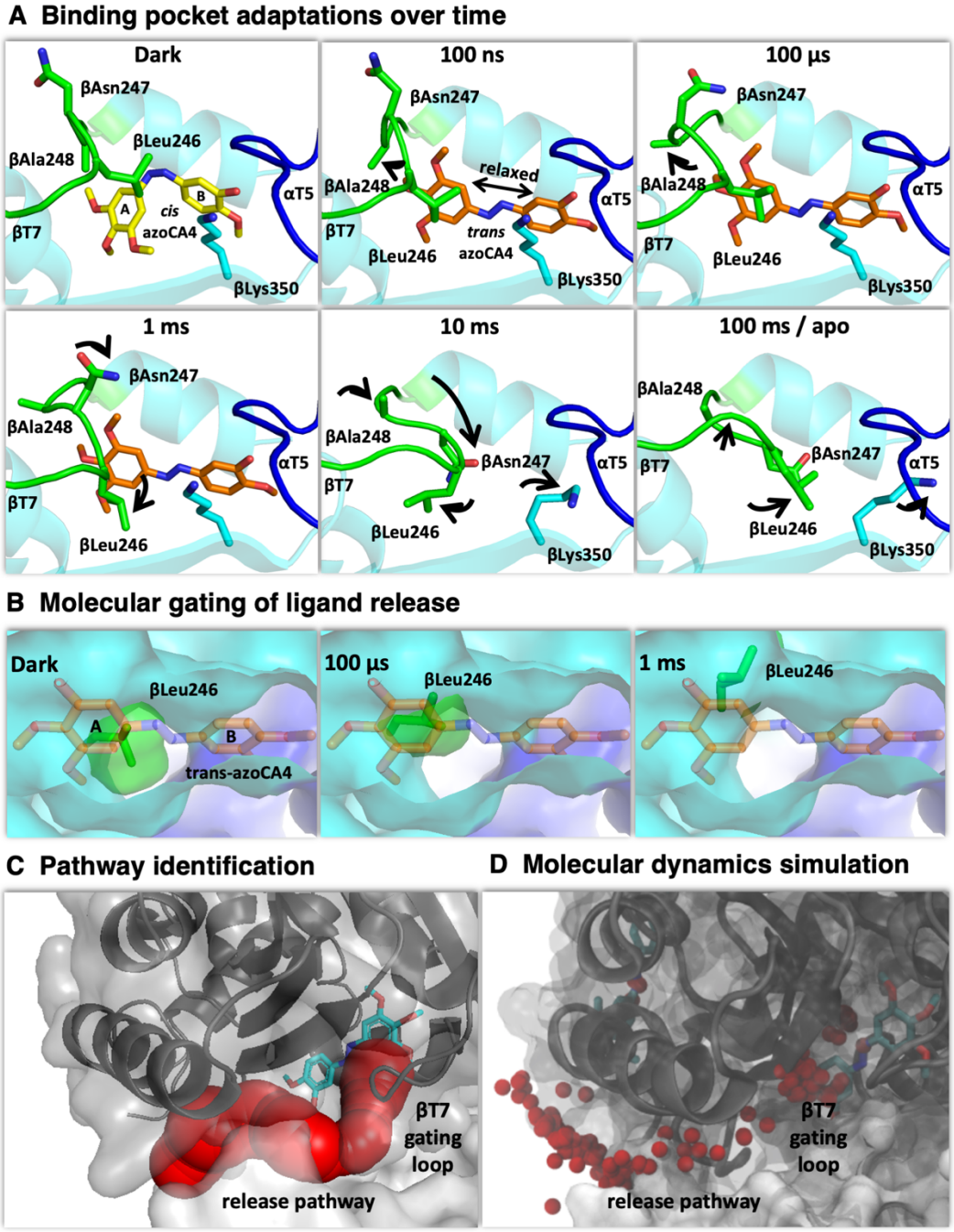


**Figure 3: Molecular changes in the βT7 gating loop allow ligand release.** (**A**) Within nanoseconds, the light induced isomerization and relaxation repositions the A ring of azo-CA4 closer to the βT7 loop (green), which acts like a lid on the colchicine-site. Further reorganizations (black arrows) in the microseconds opens a channel between the βH8 helix and the βT7 loop. In the millisecond range, the βT7 loop is folded back and packs against residues of the empty binding pocket. (**B**) Opening of a release pathway through relocation of the βT7 loop in the 1 ms structure is illustrated by the position of βLeu246 (green sticks and surface) at the indicated time delays. (**C**) The release pathway (red spheres) plotted onto the 1 ms structure. (**D**) The experimentally deduced unbinding pathway of azo-CA4 is confirmed by MD simulations. The small red spheres depict the centers of masses of ligand atoms, plotted every 50 frames along the simulation.

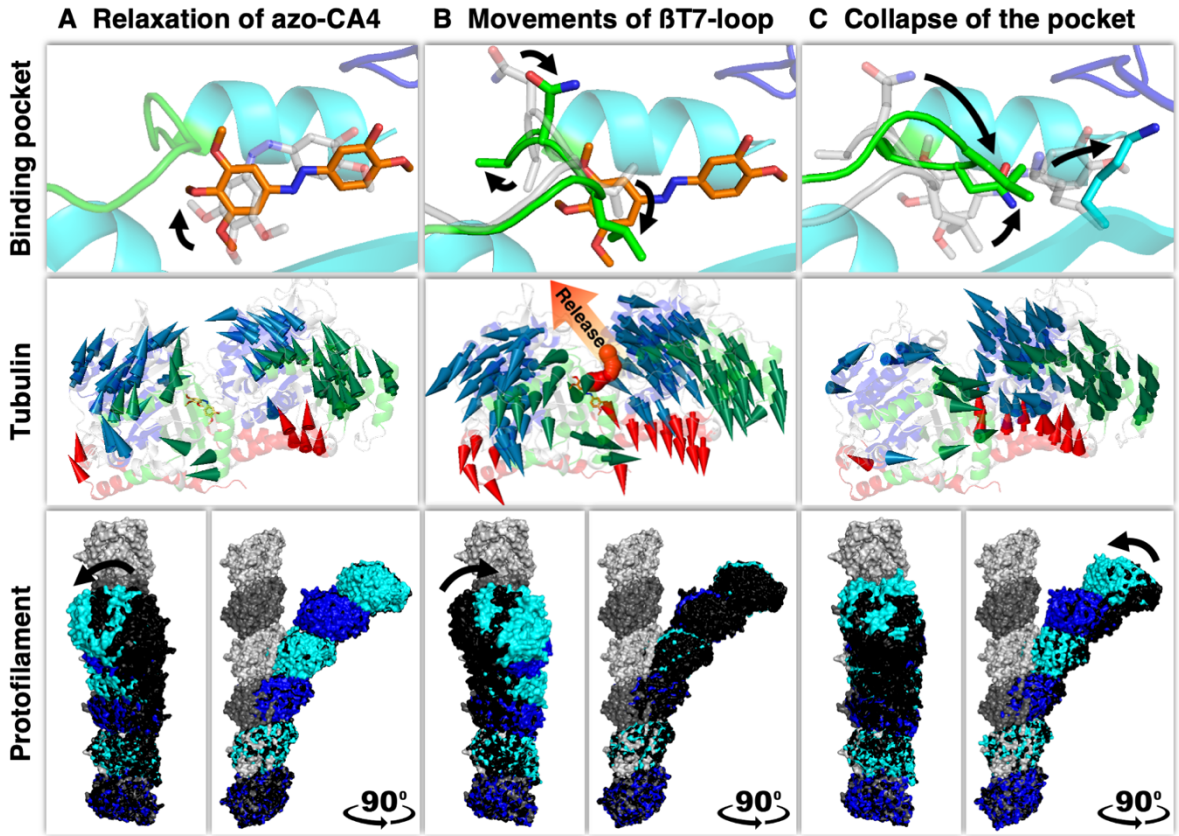


**Figure 4: Correlation between colchicine-site dynamics and global tubulin backbone rearrangements**. (**A**) Relaxation of azo-CA4: dark to 100 ns. (**B**) Movements of βT7 loop: 100 ns to 1 ms. (**C**) Collapse of the colchicine-site: 1 ms to 100 ms. The three rows depict conformational changes at different spatial levels: Binding pocket in the upper row, tubulin backbone in the middle row, and longitudinally aligned tubulin dimers in the lower row. Starting structures are shown in grey. Backbone movements within tubulin (middle row) are represented by modevectors between consecutive time delays. Every second Cα-backbone atom in the main secondary structural elements with a displacement of at least 0.5 Å is shown. The N-terminal nucleotide-binding domains, the C-terminal domains, and the intermediate domains for both α and β tubulin are shown in blue, red, and green, respectively. The release pathway (red spheres) was added to illustrate the directional movements of the tubulin subunits. The global conformational changes (lower row) are visualized by three longitudinally aligned tubulin dimers ("Straight" tubulin dimers as found in the main shaft of a microtubule are shown in surface representation (dark gray, α-tubulin; light grey, β-tubulin; PDB ID 5SYE); "Curved" tubulin dimers (α-tubulin in blue and β-tubulin in cyan) at the indicated time delay and in relation to the previous state are shown in black). Deviations demonstrate the conformational plasticity of tubulin during azo-CA4 relaxation in its binding pocket and βT7-loop movements of β-tubulin, as well as a directed curvature adjustment after azo-CA4 release. Arrows indicate the main directions of movements in the indicated time delays.